

1 **TRPML1 gating modulation by allosteric mutations and lipids**

2  
3 Ninghai Gan<sup>1,2</sup>, Yan Han<sup>2</sup>, Weizhong Zeng<sup>1,2</sup> & Youxing Jiang<sup>1,2</sup>

4  
5  
6 **Affiliations:**

7  
8 <sup>1</sup> Howard Hughes Medical Institute and Department of Physiology, University of Texas  
9 Southwestern Medical Center, Dallas, Texas, USA

10 <sup>2</sup> Department of Biophysics, University of Texas Southwestern Medical Center, Dallas, Texas,  
11 USA

12 \*Correspondence to:

13 Youxing Jiang, Ph.D., Department of Physiology, UT Southwestern Medical Center, 5323 Harry  
14 Hines Blvd., Dallas, Texas 75390-9040, Tel. 214 645-6027; Fax. 214 645-6042; E-Mail:

15 [youxing.jiang@utsouthwestern.edu](mailto:youxing.jiang@utsouthwestern.edu)

16  
17  
18  
19  
20  
21  
22  
23  
24  
25  
26  
27  
28  
29  
30

31 **Abstract:**

32 Transient Receptor Potential Mucolipin 1 (TRPML1) is a lysosomal cation channel whose loss-  
33 of-function mutations directly cause the lysosomal storage disorder mucopolidosis type IV  
34 (MLIV). TRPML1 can be allosterically regulated by various ligands including natural lipids and  
35 small synthetic molecules and the channel undergoes a global movement propagated from  
36 ligand-induced local conformational changes upon activation. In this study, we identified a  
37 functionally critical residue, Tyr404, at the C-terminus of the S4 helix, whose mutations to  
38 tryptophan and alanine yield gain- and loss-of-function channels, respectively. These allosteric  
39 mutations mimic the ligand activation or inhibition of the TRPML1 channel without interfering  
40 with ligand binding and both mutant channels are susceptible to agonist or antagonist modulation,  
41 making them better targets for screening potent TRPML1 activators and inhibitors. We also  
42 determined the high-resolution structure of TRPML1 in complex with the PI(4,5)P<sub>2</sub> inhibitor,  
43 revealing the structural basis underlying this lipid inhibition. In addition, an endogenous  
44 phospholipid likely from sphingomyelin is identified in the PI(4,5)P<sub>2</sub>-bound TRPML1 structure  
45 at the same hotspot for agonists and antagonists, providing a plausible structural explanation for  
46 the inhibitory effect of sphingomyelin on agonist activation.

47

48 **Introduction:**

49 Transient Receptor Potential Mucolipin 1 (TRPML1) is a Ca<sup>2+</sup>-permeable, non-selective,  
50 lysosomal cation channel ubiquitously expressed in mammalian cells (Dong *et al*, 2008;  
51 LaPlante *et al*, 2002; Sun *et al*, 2000). TRPML1 plays critical roles in many important cellular  
52 activities including lipid accumulation (Shen *et al*, 2012), signaling transduction (Kilpatrick *et al*,  
53 2016), lysosome trafficking (Venkatachalam *et al*, 2015), and autophagy (Scotto Rosato *et al*,  
54 2019). The loss-of-function mutations in TRPML1 directly cause the lysosomal storage disorder  
55 mucopolidosis type IV (MLIV), a neurodegenerative disease characterized by abnormal  
56 neurodevelopment, retinal degeneration, and iron-deficiency anemia (Bargal *et al*, 2000; Bassi *et*  
57 *al*, 2000; Gan & Jiang, 2022; Nilius *et al*, 2007). Because of its physiological importance and  
58 direct disease association, TRPML1 has been extensively studied and is a potential target for  
59 drug development.

60 TRPML1 can be regulated by various ligands including both natural lipids and small  
61 synthetic molecules. The channel can be activated by the lysosome-specific phosphatidylinositol

62 3,5-bisphosphate (PI(3,5)P<sub>2</sub>) (Dong *et al.*, 2010), but inhibited by the plasma membrane-enriched  
63 PI(4,5)P<sub>2</sub> (Zhang *et al.*, 2012). Given its pharmacological importance, many synthetic agonists  
64 and antagonists have been developed for TRPML1 activation and inhibition (Chen *et al.*, 2014;  
65 Grimm *et al.*, 2010; Samie *et al.*, 2013; Shen *et al.*, 2012). Interestingly, the mTOR (Mammalian  
66 target of rapamycin) inhibitor rapamycin and its derivatives can also synergistically activate  
67 TRPML1 with PI(3,5)P<sub>2</sub> (Gan *et al.*, 2022; Zhang *et al.*, 2019). Recent studies also suggest that  
68 sphingomyelin, a major membrane component, can also modulate the TRPML1 activation (Prat  
69 Castro *et al.*, 2022; Shen *et al.*, 2012).

70 Several TRPML1 channel structures in both open and closed conformations with various  
71 ligands have been determined (Chen *et al.*, 2017; Fine *et al.*, 2018; Gan *et al.*, 2022; Schmiede *et al.*  
72 *et al.*, 2017; Schmiede *et al.*, 2021), revealing some unique features of the TRPML1 channel. Firstly,  
73 all ligand-binding sites in the structures converge to two hot spots: The N-terminal poly-basic  
74 pocket for PIP<sub>2</sub> and the inter-subunit interface in the middle of the membrane between S5 and S6  
75 for agonists, antagonists, and rapamycin (Fine *et al.*, 2018; Gan *et al.*, 2022; Schmiede *et al.*,  
76 2017; Schmiede *et al.*, 2021) (Figure 1a). Secondly, all open TRPML1 structures are almost  
77 identical regardless of the activation stimuli. Thirdly, structural comparison between the open  
78 and closed conformation illustrates that TRPML1 gating is not merely a local conformational  
79 change but involves the global movement of almost the entire channel mediated by tight inter-  
80 and intra-subunit packing within the channel tetramer (Movie supplement 1). Finally, the  
81 necessity of global movement for channel activation underlies the allosteric regulation of  
82 TRPML1 by two distantly bound ligands - that is, the ligand-induced local conformational  
83 change at one site can propagate to the other site and thereby affect the binding of the other  
84 ligand (Gan *et al.*, 2022). The high allostery of TRPML1 gating would allow us to design  
85 allosteric mutations that are remote from the channel pore but can still stabilize the channel in an  
86 open or closed state, mimicking the ligand activation or inhibition of the channel. To this end,  
87 we identified Tyr404 on the S4 helix as an allosteric site whose mutation can promote or inhibit  
88 TRPML1 gating. Furthermore, we also determined a high-resolution structure of PI(4,5)P<sub>2</sub>-  
89 inhibited TRPML1 and demonstrated that in addition to competing against PI(3,5)P<sub>2</sub> activator for  
90 the same site, PI(4,5)P<sub>2</sub> also allosteric inhibits small molecule agonist by stabilize the channel in  
91 the closed conformation. Furthermore, the high-resolution PI(4,5)P<sub>2</sub>-bound TRPML1 structure

92 also revealed a bound phospholipid likely from sphingomyelin at the agonist/antagonist site,  
93 providing a plausible explanation for sphingomyelin inhibition of TRPML1.

94

## 95 **Results:**

### 96 **Allosteric mutations at Tyr404 recapitulate TRPML1 gating**

97 Our previous study on the allosteric activation of TRPML1 by PI(3,5)P<sub>2</sub> and rapamycin  
98 demonstrated that ligand-induced local conformational changes can propagate to distal parts of  
99 the channel through tight inter- and intra-subunit packing within the channel tetramer, allowing  
100 the channel to integrate the stimuli from these two distantly bound ligands. The PI(3,5)P<sub>2</sub> and  
101 rapamycin-induced local conformational changes converge to the same driving force on S4 helix,  
102 resulting in a slight bend of the C-terminal half of the S4 that facilitates the channel opening  
103 (Gan *et al.*, 2022) (Figure 1b). A key interaction coupled to the S4 bending movement is the  
104 insertion of Tyr404 side chain into a pocket surrounded by S1, S3, and S4 helices where its  
105 aromatic ring is sandwiched between the side chains of Leu66 and Arg403. We hypothesized  
106 that mutations at Tyr404 that stabilize its sidechain in the pocket would facilitate channel  
107 activation; conversely, mutations that destabilize its sidechain in the pocket would negatively  
108 modulate the channel activation. To test this, we replaced Tyr404 with tryptophan and alanine,  
109 respectively, and measured the effect of these mutations on channel activity. As illustrated in the  
110 electrophysiological recordings using whole-cell patches, the Y404W mutant elicits large  
111 inward-rectifying currents without any ligands, indicating that Y404W is a gain-of-function  
112 (GOF) mutant (Figure 1c and Figure supplement 1a). Adding extra activation ligands such as  
113 PI(3,5)P<sub>2</sub>, rapamycin, or small molecule agonist ML-SA1 only marginally increases the currents.  
114 The Y404W GOF mutant mimics a ligand-activated channel, yet its mutation site is remote from  
115 the pore domain and the channel can still be allosterically inhibited by small molecule  
116 antagonists (ML-SI1 and ML-SI3) (Figure 1d and Figure supplement 1b). This is distinct from  
117 other gain-of-function mutants in which proline substitutions on the S5 helix lock the pore in an  
118 open state and the channels are no longer susceptible to antagonist inhibition (Dong *et al.*, 2009;  
119 Grimm *et al.*, 2007; Kim *et al.*, 2007; Nagata *et al.*, 2008; Xu *et al.*, 2007).

120 Y404A, on the other hand, represents a loss-of-function mutant and elicits much lower  
121 currents even in the presence of potent agonist ML-SA1 (Figure 1e and Figure supplement 1c).

122 While ML-SA1 can potently activate the wild-type TRPML1 channel, the Y404A mutation  
123 mimics PI(4,5)P<sub>2</sub> inhibition and allosterically inhibits ML-SA1 binding, significantly decreasing  
124 the efficacy of ML-SA1 activation (Figure 1f & g).

### 125 **Structure of GOF Y404W mutant**

126 To reveal the structural basis underlying the channel activation of the Y404W mutant, we  
127 determined its structure in the absence of any ligands to 2.86 Å resolution (Figure supplement 2-  
128 3 and Methods). As expected, the Y404W mutant adopts an open conformation with a structure  
129 almost identical to other ligand-activated open TRPML1, consistent with its GOF property  
130 (Figure 2a and Figure supplement 3b). Like Tyr404 in the wide-type open TRPML1, the side  
131 chain of W404 in the mutant is inserted into the pocket surrounded by S1, S3, and S4 helices and  
132 sandwiched between Leu66 and Arg403 (Figure 2b). However, the larger indole ring of Trp404  
133 provides a better spatial fitting into the pocket than the phenol ring of Tyr404 and several  
134 surrounding residues (Lys65, Gln69, and Leu358) provide extra van der Waals contacts to the  
135 Trp404 side chain. Thus, by enhancing the stability of the aromatic side chain inside the pocket,  
136 Y404W mutation facilitates the bending of S4 which in turn propagates to the pore through the  
137 S4-S5 linker and activates the channel (Gan *et al.*, 2022). The Y404W mutant structure  
138 demonstrates that the sidechain packing in the pocket is essential for stabilizing the open channel  
139 and the lack of such packing capacity in the Y404A mutant with a small side-chain likely  
140 destabilizes the open conformation, yielding a loss-of-function channel. It is worth noting that  
141 Arg403 plays two essential roles in TRPML1 gating: its side chain is part of the pocket that  
142 stabilizes Tyr404 in the open state; its guanidinium group forms a salt bridge with the C3  
143 phosphate group of PI(3,5)P<sub>2</sub> upon ligand activation (Gan *et al.*, 2022). As expected, Arg403 is  
144 highly conserved in the TRPML channel family, and its R403C variant identified in an MLIV  
145 patient is a loss-of-function mutant (Chen *et al.*, 2014).

146

### 147 **Structure of TRPML1 in PI(4,5)P<sub>2</sub>-bound closed state**

148 While PI(4,5)P<sub>2</sub> inhibits PI(3,5)P<sub>2</sub> activation of TRPML1 by directly competing for the  
149 same binding site, it also allosterically inhibits the agonist-activated channel (Chen *et al.*, 2017),  
150 suggesting that PI(4,5)P<sub>2</sub> binding stabilizes the TRPML1 channel in a closed conformation. A  
151 previous low-resolution structure of TRPML1 in complex with PI(4,5)P<sub>2</sub> revealed the

152 approximate location of PI(4,5)P<sub>2</sub> binding but failed to explain how its binding stabilizes the  
153 channel in the closed state and allosterically inhibits the agonist-activated channel (Fine *et al.*,  
154 2018). To address this, we determined the structure of PI(4,5)P<sub>2</sub>-bound TRPML1 at 2.46 Å  
155 (Figure 3a, Figure supplement 3-5 and Methods). The density from the IP3 head group of  
156 PI(4,5)P<sub>2</sub>, especially the phosphate groups on C4 and C5 of the inositol, can be clearly defined in  
157 the EM map (Figure 3a-3c). The phosphatidyl group, however, is flexible and could not be  
158 resolved in the structure. While PI(4,5)P<sub>2</sub> binding overlaps with that of PI(3,5)P<sub>2</sub>, their IP3 head  
159 group positions are quite different (Figure 3b-3e). In the PI(3,5)P<sub>2</sub>-bound structure (Figure 3d),  
160 the head group protrudes deep into the N-terminal PIP<sub>2</sub>-binding pocket enclosed by two short  
161 clamp-shaped helices of H1 and H2, and the cytosolic ends of S1 and S2 helices, allowing its C3  
162 phosphate to engage in direct interactions with Arg403 and Tyr355 to facilitate channel  
163 activation (Gan *et al.*, 2022). These C3 phosphate-mediated interactions are absent in PI(4,5)P<sub>2</sub>-  
164 bound structure. Instead, the head group of PI(4,5)P<sub>2</sub> is trapped at the entrance of the pocket and  
165 forms a bridge between S1 and S2 with its phosphate groups stabilized by positively charged  
166 residues from H2, S1, and S2 (Figure 3b & 3c). A major conformational change between the  
167 open and closed states is an upward movement of the S1 helix, a prerequisite for Tyr404  
168 insertion between Leu66 and Arg403 and the subsequent bending of S4 (Figure 3e). Therefore,  
169 the PI(4,5)P<sub>2</sub>-mediated bridging interaction between S1 and S2 would hinder the S1 movement  
170 and stabilize the channel in the closed conformation, exerting allosteric inhibition on agonist  
171 activation.

172

### 173 **Endogenous sphingomyelin lipid at the agonist- and antagonist-binding site**

174 The high-resolution structure of PI(4,5)P<sub>2</sub>-bound closed TRPML1 also reveals a well-defined  
175 density from an endogenous lipid molecule at the inter-subunit interface between S5 and S6  
176 (Figure 4a). The lipid contains a choline head group and is likely a phosphatidylcholine (PC) or  
177 sphingomyelin (SM), the two main choline-containing phospholipid components of the outer  
178 leaflet of the plasma membrane. The tail from one of the lipid alkyl chains penetrates deep into  
179 an inter-subunit pocket in the middle of the membrane, overlapping with the hotspot for both  
180 channel agonist and antagonist (Figure supplement 6). This alkyl chain has to be displaced upon  
181 agonist or antagonist binding, suggesting that the lipid occupation would compete against agonist  
182 or antagonist binding. We suspect this bound lipid is sphingomyelin which is also enriched in the

183 endocytic recycling compartment and has been shown to inhibit TRPML1 activity (Prat Castro *et*  
184 *al.*, 2022; Schuchman, 2010; Shen *et al.*, 2012; Slotte, 2013). Key evidence to support SM  
185 inhibition is that its enrichment can reduce the agonist (i.e. SF-51 and ML-SA1) activation of  
186 TRPML1 (Shen *et al.*, 2012). Indeed, we did observe the reduction of SF-51-activated TRPML1  
187 current upon SM enrichment (Figure 4b and Figure supplement 7a). However, based on our  
188 structure, we hypothesize that the role of sphingomyelin is to stabilize rather than directly inhibit  
189 the channel; the SM inhibition upon enrichment is an indirect effect attributable to its  
190 competition against agonist binding that reduces the apparent efficacy of agonist activation. This  
191 hypothesis would imply that SM can also function as an indirect activator by competing against  
192 antagonists and reducing their effectiveness in channel inhibition. The gain-of-function Y404W  
193 mutant, which is still susceptible to antagonist inhibition, provides a good system to test that. As  
194 shown in Figure 4c and Figure supplement 7b, SM shows no obvious inhibition to the mutant  
195 channel activity whereas antagonist ML-SI1 markedly reduces the mutant channel current; upon  
196 SM enrichment, ML-SI1 inhibition is mitigated resulting in a recovery of the channel current.  
197 This observation confirms the competitive binding of SM at the hot spot for both agonists and  
198 antagonists.

199

## 200 **Summary**

201 In this study, we designed and analyzed the allosteric mutations at Tyr404 that recapitulate the  
202 gating of TRPML1. Replacing this tyrosine with tryptophan or alanine stabilizes or destabilizes  
203 the channel in the open state, yielding a gain- or loss-of-function mutant. The structure of the  
204 Y404W mutant adopts the same open structure as ligand-activated TRPML1, once again  
205 highlighting the global conformational change for TRPML1 channel activation. As Tyr404 is  
206 distant from the hot spots for ligand binding, the two gain- and loss-of-function mutants can still  
207 be allosterically modulated by antagonists and agonists. Thus, these allosteric mutants can mimic  
208 ligand-activated or inhibited TRPML1 without interfering with ligand binding, making them  
209 better targets for screening potent small molecule TRPML1 inhibitors and activators. We also  
210 investigated the structural basis of PI(4,5)P<sub>2</sub> inhibition of TRPML1 by determining the PI(4,5)P<sub>2</sub>-  
211 bound structure, revealing a different binding mode by its head group at the N-terminal polybasic  
212 site than that of PI(3,5)P<sub>2</sub>. The head group of PI(4,5)P<sub>2</sub> mediates a bridging interaction between

213 S1 and S2 and stabilizes TRPML1 in a closed conformation. In the high-resolution PI(4,5)P<sub>2</sub>-  
214 bound TRPML1 structure, we also visualize clear density from a choline-containing  
215 phospholipid at the same site for agonists or antagonists. In light of its high membrane  
216 abundance and competing effect on agonist activation and antagonist inhibition, this bound lipid  
217 is likely from sphingomyelin.

218

219

220



## 221 **Methods:**

### 222 **Protein expression and purification**

223 Protein expression and purification were performed as previously described (Gan *et al.*, 2022).  
224 The *Mus musculus* TRPML1 gene with a C-terminal thrombin cleavage site and a 10× His tag  
225 was cloned into a pEZTBM vector (Morales-Perez *et al.*, 2016) and heterologously expressed in  
226 HEK293F cells using the BacMam system. The baculovirus was produced in Sf9 cells and used  
227 to transduce the HEK293F cells at a ratio of 1:40 (virus:HEK293F, v/v) and supplemented with  
228 1 mM sodium butyrate to boost the protein expression. Cells were cultured in suspension at  
229 37 °C for 48 h and harvested by centrifugation at 3,000g. All purification procedures were  
230 carried out at 4 °C unless specified otherwise. The cell pellet was re-suspended in buffer A  
231 (20 mM Tris pH 8.0, 150mM NaCl) supplemented with a protease inhibitor cocktail (containing  
232 1 mg ml<sup>-1</sup> each of DNase, pepstatin, leupeptin, and aprotinin and 1 mM PMSF) and  
233 homogenized by sonication on ice. Protein was extracted with 1% (w/v) n-dodecyl-β-D-  
234 maltopyranoside (DDM; Anatrace) supplemented with 0.2% (w/v) cholesteryl hemisuccinate  
235 (CHS; Sigma-Aldrich) by gentle agitation for 2 h. After extraction, the supernatant was collected  
236 after a 1 h centrifugation at 48,000g and incubated with Ni-NTA resin and 20 mM imidazole  
237 with gentle agitation. After 1 h, the resin was collected on a disposable gravity column (Bio-Rad),  
238 washed with buffer B (buffer A + 0.04% glyco-diosgenin (GDN; Anatrace) ) with 20 mM  
239 imidazole. The washed resin was left on-column in buffer B and digested with thrombin  
240 overnight. After digestion, the flow-through was concentrated, and purified by size-exclusion  
241 chromatography on a Superose 6 10/300 GL column (GE Healthcare) pre-equilibrated with buffer  
242 B. The protein peak was collected and concentrated. For PI(4,5)P<sub>2</sub>-bound structure, purified  
243 protein was incubated with 0.5mM PI(4,5)P<sub>2</sub> on ice for 4 h. The lipid ligand used in this study is  
244 PI(4,5)P<sub>2</sub> diC8 (Echelon)

### 245 **Electron microscopy data acquisition**

246 Electron microscopy data acquisition followed the protocol previously described (Gan *et al.*,  
247 2022). The cryo-EM grids were prepared by applying 3.5 μl protein (3.5 mg/mL) to a glow-  
248 discharged Quantifoil R1.2/1.3 200-mesh copper holey carbon grid (Quantifoil, Micro Tools  
249 GmbH) and blotted for 3.0 s under 100% humidity at 4 °C before being plunged into liquid  
250 ethane using a Mark IV Vitrobot (FEI). For the dataset of Y404W, micrographs were acquired

251 on a Titan Krios microscope (FEI) operated at 300 kV with a K3 Summit direct electron detector  
252 (Gatan), using a slit width of 20 eV on a GIF-Quantum energy filter. Data were collected using  
253 CDS (Correlated Double Sampling) mode of the K3 camera with a super resolution pixel size of  
254 0.413 Å. The defocus range was set from  $-0.9$  to  $-2.2$   $\mu\text{m}$ . Each movie was dose-fractionated to  
255 60 frames with a dose rate of  $1\text{e-}/\text{\AA}^2/\text{frame}$  for a total dose of  $60\text{e-}/\text{\AA}^2$ . The total exposure time  
256 was between 5 to 6 s. For the PI(4,5)P<sub>2</sub>-bound dataset, micrographs were acquired on a Titan  
257 Krios microscope (FEI) operated at 300 kV with a Falcon4 electron detector (Thermo Fisher),  
258 using a slit width of 20 eV on a post-column Selectris X energy filter (Thermo Fisher Scientific).  
259 Data was collected using Falcon 4 camera with a pixel size of 0.738 Å. The defocus range was  
260 set from  $-0.9$  to  $-2.2$   $\mu\text{m}$ . Each movie was dose-fractionated to 60 frames with a dose rate of  $1\text{e-}$   
261  $/\text{\AA}^2/\text{frame}$  for a total dose of  $60\text{e-}/\text{\AA}^2$ . The total exposure time was between 3.5 to 4 s.

262

## 263 **Image processing**

264 Images were processed as previously described (Gan *et al.*, 2022). Movie frames were motion  
265 corrected and binned two times and dose-weighted using MotionCor2 (Zheng *et al.*, 2017). The  
266 CTF parameters of the micrographs were estimated using the GCTF program (Zhang, 2016). The  
267 rest of the image processing steps were carried out using RELION 3.1 (Nakane *et al.*, 2020;  
268 Scheres, 2012; Zivanov *et al.*, 2018). All resolution was reported according to the gold-standard  
269 Fourier shell correlation (FSC) using the 0.143 criterion (Henderson *et al.*, 2012). Local  
270 resolution was estimated using Relion. Aligned micrographs were manually inspected to remove  
271 those with ice contamination and bad defocus. Particles were selected using Gautomatch (K.  
272 Zhang, MRC LMB, [https://www2.mrc-lmb.cam.ac.uk/research/locally-developed-](https://www2.mrc-lmb.cam.ac.uk/research/locally-developed-software/zhang-software/)  
273 [software/zhang-software/](https://www2.mrc-lmb.cam.ac.uk/research/locally-developed-software/zhang-software/)) and extracted using a binning factor of 3. 2D classification was  
274 performed in Relion 3.1. Selected particles after 2D classification were subjected to one around  
275 3D classification. The mouse TRPML1 map (EMD-8883 (Chen *et al.*, 2017)) low-pass filtered to  
276 30 Å was used as the initial reference. Classes that showed clear features of the TRPML1  
277 channel were combined and subjected to 3D auto-refinement and another round of 3D  
278 classification without performing particle alignment using a soft mask around the protein portion  
279 of the density. The best resolving classes were then re-extracted with the original pixel size and  
280 further refined. Beam tilt, anisotropic magnification, and per-particle CTF estimations and

281 Bayesian polishing were performed in Relion 3.1 to improve the resolution of the final  
282 reconstruction.

283 For the Y404W structure dataset, a total of 4,724 movies were collected and 4,505 were selected  
284 after motion correction and CTF estimation. A total number of 864,698 particles were extracted  
285 from the selected micrographs and were subjected to one round of 2D classification, from which  
286 87,846 particles were selected. After the initial 3D classification, 35,460 particles were selected  
287 and subjected to a 3D auto-refinement job and further ctf refinements, yielding a map at 2.86Å  
288 overall resolution (Figure supplement 2).

289 For the PI(4,5)P<sub>2</sub>-bound dataset, a total of 8,164 movies were collected and 7,895 were selected  
290 after motion correction and CTF estimation. A total number of 1,065,778 particles were  
291 extracted from the selected micrographs and were subjected to one round of 2D classification,  
292 from which 555,281 particles were selected. After the initial 3D classification, 359,441 particles  
293 were selected and subjected to a 3D auto-refinement job. Next, a soft mask excluding the micelle  
294 density was applied and particles were sorted into 5 classes without performing alignment. From  
295 this, one classe with a total number of 60,597 particles were selected and further refined. In the  
296 postprocess step, a B-factor of -60 was manually given, yielding a map at 2.46Å overall  
297 resolution (Figure supplement 4).

## 298 **Model building, refinement and validation**

299 Model building, refinement and validation followed the previously described protocol (Gan *et al.*,  
300 2022). The structure of mouse TRPML1 (PDB code: 5WPV) was used as the initial model and  
301 was manually adjusted in Coot (Emsley *et al.*, 2010) and refined against the map by using the real  
302 space refinement module with secondary structure and non-crystallographic symmetry restraints  
303 in the Phenix package (Adams *et al.*, 2010). The final structure model of Y404W includes  
304 residues 40-200, 216-527. The final structure model of the PI(4,5)P<sub>2</sub>-bound includes residues 39-  
305 200, 216-285, 296-527. About 40 residues at the amino terminus and 50 residues at the carboxy  
306 terminus are disordered and not modeled. The statistics of the geometries of the models were  
307 generated using MolProbity (Chen *et al.*, 2010). All the figures were prepared in PyMol  
308 (Schrödinger, LLC.), UCSF Chimera (Pettersen *et al.*, 2004). Pore radii were calculated using the  
309 HOLE program (Smart *et al.*, 1996).

## 310 **Electrophysiology**

311 Electrophysiology was carried out following a previously described protocol with minor  
312 modifications (Gan *et al.*, 2022). For electrophysiological analysis, the two di-leucine motifs  
313 (15<sub>LL</sub> and 577<sub>LL</sub>) of mouse TRPML1 responsible for lysosomal targeting were replaced with  
314 alanines to facilitate the trafficking of the channel to the plasma membrane (Grimm *et al.*, 2010;  
315 Vergarajauregui & Puertollano, 2006). The N-terminal GFP tagged, plasma membrane-targeting  
316 TRPML1 mutant (TRPML1-4A) and derived point mutations were overexpressed in HEK293  
317 cells and the channel activities were directly measured by patching the plasma membrane. In this  
318 setting, the extracellular side is equivalent to the luminal side of TRPML1 in endosomes or  
319 lysosomes. 48 h after transfection, cells were dissociated by trypsin treatment and kept in  
320 complete serum-containing medium; the cells were re-plated onto 35 mm tissue culture dishes  
321 and kept in a tissue culture incubator until recording. Patch clamp in the whole-cell or inside-out  
322 configuration was used to measure TRPML1 activity on the HEK plasma membrane. The  
323 standard bath solution for whole cell current recording contained (in mM): 145 sodium  
324 methanesulfonate, 5 NaCl, 1 MgCl<sub>2</sub>, 10 HEPES buffered with Tris, pH 7.4; and the pipette  
325 solution contained (in mM): 140 caesium methanesulfonate, 5 NaCl, 5 MgCl<sub>2</sub>, 10 EGTA, 10  
326 HEPES buffered with Tris, pH 7.4. The bath solution for inside-out configuration contained (in  
327 mM): 140 potassium methanesulfonate, 5 NaCl, 2 MgCl<sub>2</sub>, 0.4 CaCl<sub>2</sub>, 1 EGTA, 10 HEPES  
328 buffered with Tris, pH 7.4; and the pipette solution contained (in mM): 145 sodium  
329 methanesulfonate, 5 NaCl, 1 MgCl<sub>2</sub>, 0.5 EGTA, 10 HEPES buffered with Tris, pH 7.4. For  
330 whole cell recording of PI(3,5)P<sub>2</sub>-activated channel, we had to include high concentration of  
331 PI(3,5)P<sub>2</sub> (100 μM) in the pipette solution (cytosolic side) in order to quickly obtain stable  
332 PI(3,5)P<sub>2</sub>-evoked current, likely because of the slow diffusion of this lipid ligand. PI(4,5)P<sub>2</sub> was  
333 added in the cytosolic side, Tem, ML-SA1, ML-SI3, ML-SI1, SM were added in the bath  
334 solution. SM competition assays with SF-51 and ML-SI1 were conducted under pH 4.6. The  
335 patch pipettes were pulled from Borosilicate glass and heat polished to a resistance of 2–5 MΩ  
336 (2–3 MΩ for inside-out patch, and 3–5 MΩ for whole-cell current recording). Data were acquired  
337 using an AxoPatch 200B amplifier (Molecular Devices) and a low-pass analogue filter set to  
338 1 kHz. The current signal was sampled at a rate of 20 kHz using a Digidata 1550B digitizer  
339 (Molecular Devices) and further analyzed with pClamp 11 software (Molecular Devices). After  
340 the patch pipette attached to the cell membrane, the giga seal (>10 GΩ) was formed by gentle

341 suction. The inside-out configuration was formed by pulling the pipette away from the cell, and  
342 the pipette tip was exposed to the air for 2 seconds. The whole-cell configuration was formed by  
343 short zap or suction to rupture the patch. The holding potential was set to 0 mV. The whole-cell  
344 and inside-out macroscopic current recordings were obtained using voltage pulses ramped from  
345 -140 mV to +50 mV over a duration of 800 ms. The sample traces for the I-V curves of  
346 macroscopic currents shown in each figure were obtained from recordings on the same patch. All  
347 data points are mean  $\pm$  s.e.m. ( $n \geq 5$ ).

348 **Data availability.** The cryo-EM density maps of mouse TRPML1 have been deposited in the  
349 Electron Microscopy Data Bank (EMDB) under accession numbers 45429 (Y404W), 45432  
350 (PI(4,5)P<sub>2</sub>-bound). Atomic coordinates have been deposited in the Protein Data Bank (PDB)  
351 under accession numbers 9CBZ (Y404W), 9CC2 (PI(4,5)P<sub>2</sub>-bound).

352 **Acknowledgments:** Cryo-EM sample grids were prepared at the Structural Biology Laboratory  
353 at the University of Texas Southwestern Medical Center which is partially supported by the  
354 CPRIT Core Facility Support Award RP170644. Single particle Cryo-EM data were collected at  
355 the University of Texas Southwestern Medical Center Cryo-EM Facility that is funded by the  
356 CPRIT Core Facility Support Award RP170644 and Pacific Northwest Center for Cryo-EM  
357 (PNCC). We thank Omar Davulcu for helping in data collection at PNCC under user proposal  
358 51776. Ninghai Gan is a HHMI fellow of the Jane Coffin Childs Memorial Fund. This work was  
359 supported in part by the Howard Hughes Medical Institute and by grants from the National  
360 Institute of Health (R35GM140892 to Y.J.) and the Welch Foundation (Grant I-1578 to Y.J.).

361  
362 **Author contributions:** N.G. prepared the samples; Y.H. and N.G. performed data acquisition,  
363 image processing, and structure determination; W.Z. performed electrophysiology recording; All  
364 authors participated in research design, data analysis, discussion, and manuscript preparation.

365  
366 **Declaration of interests:** The authors declare no competing financial interests.

367  
368

## 369 Reference

- 370 Adams PD, Afonine PV, Bunkóczi G, Chen VB, Davis IW, Echols N, Headd JJ, Hung LW,  
371 Kapral GJ, Grosse-Kunstleve RW *et al* (2010) PHENIX: a comprehensive Python-based system  
372 for macromolecular structure solution. *Acta Crystallogr D Biol Crystallogr* 66: 213-221
- 373 Bargal R, Avidan N, Ben-Asher E, Olender Z, Zeigler M, Frumkin A, Raas-Rothschild A,  
374 Glusman G, Lancet D, Bach G (2000) Identification of the gene causing mucopolipidosis type IV.  
375 *Nat Genet* 26: 118-123
- 376 Bassi MT, Manzoni M, Monti E, Pizzo MT, Ballabio A, Borsani G (2000) Cloning of the gene  
377 encoding a novel integral membrane protein, mucopolipidin and identification of the two major  
378 founder mutations causing mucopolipidosis type IV. *Am J Hum Genet* 67: 1110-1120
- 379 Chen CC, Keller M, Hess M, Schiffmann R, Urban N, Wolfgardt A, Schaefer M, Bracher F, Biel  
380 M, Wahl-Schott C *et al* (2014) A small molecule restores function to TRPML1 mutant isoforms  
381 responsible for mucopolipidosis type IV. *Nat Commun* 5: 4681
- 382 Chen Q, She J, Zeng W, Guo J, Xu H, Bai X-c, Jiang Y (2017) Structure of mammalian  
383 endolysosomal TRPML1 channel in nanodiscs. *Nature* 550: 415-418
- 384 Chen VB, Arendall WB, 3rd, Headd JJ, Keedy DA, Immormino RM, Kapral GJ, Murray LW,  
385 Richardson JS, Richardson DC (2010) MolProbity: all-atom structure validation for  
386 macromolecular crystallography. *Acta Crystallogr D Biol Crystallogr* 66: 12-21
- 387 Dong XP, Cheng X, Mills E, Delling M, Wang F, Kurz T, Xu H (2008) The type IV mucopolipidosis-  
388 associated protein TRPML1 is an endolysosomal iron release channel. *Nature* 455: 992-996
- 389 Dong XP, Shen D, Wang X, Dawson T, Li X, Zhang Q, Cheng X, Zhang Y, Weisman LS, Delling  
390 M *et al* (2010) PI(3,5)P(2) controls membrane trafficking by direct activation of mucolipin Ca(2+)-  
391 release channels in the endolysosome. *Nat Commun* 1: 38
- 392 Dong XP, Wang X, Shen D, Chen S, Liu M, Wang Y, Mills E, Cheng X, Delling M, Xu H (2009)  
393 Activating mutations of the TRPML1 channel revealed by proline-scanning mutagenesis. *J Biol*  
394 *Chem* 284: 32040-32052
- 395 Emsley P, Lohkamp B, Scott WG, Cowtan K (2010) Features and development of Coot. *Acta*  
396 *Crystallogr D Biol Crystallogr* 66: 486-501
- 397 Fine M, Schmiede P, Li X (2018) Structural basis for PtdInsP(2)-mediated human TRPML1  
398 regulation. *Nat Commun* 9: 4192
- 399 Gan N, Han Y, Zeng W, Wang Y, Xue J, Jiang Y (2022) Structural mechanism of allosteric  
400 activation of TRPML1 by PI(3,5)P(2) and rapamycin. *Proc Natl Acad Sci U S A* 119
- 401 Gan N, Jiang Y (2022) Structural biology of cation channels important for lysosomal calcium  
402 release. *Cell Calcium* 101: 102519
- 403 Grimm C, Cuajungco MP, van Aken AF, Schnee M, Jörs S, Kros CJ, Ricci AJ, Heller S (2007) A  
404 helix-breaking mutation in TRPML3 leads to constitutive activity underlying deafness in the  
405 varitint-waddler mouse. *Proc Natl Acad Sci U S A* 104: 19583-19588
- 406 Grimm C, Jörs S, Saldanha SA, Obukhov AG, Pan B, Oshima K, Cuajungco MP, Chase P,  
407 Hodder P, Heller S (2010) Small molecule activators of TRPML3. *Chem Biol* 17: 135-148
- 408 Henderson R, Sali A, Baker ML, Carragher B, Devkota B, Downing KH, Egelman EH, Feng Z,  
409 Frank J, Grigorieff N *et al* (2012) Outcome of the first electron microscopy validation task force  
410 meeting. *Structure* 20: 205-214
- 411 Kilpatrick BS, Yates E, Grimm C, Schapira AH, Patel S (2016) Endo-lysosomal TRP mucolipin-1  
412 channels trigger global ER Ca<sup>2+</sup> release and Ca<sup>2+</sup> influx. *J Cell Sci* 129: 3859-3867
- 413 Kim HJ, Li Q, Tjon-Kon-Sang S, So I, Kiselyov K, Muallem S (2007) Gain-of-function mutation in  
414 TRPML3 causes the mouse Varitint-Waddler phenotype. *J Biol Chem* 282: 36138-36142
- 415 LaPlante JM, Falardeau J, Sun M, Kanazirska M, Brown EM, Slaugenhaupt SA, Vassilev PM  
416 (2002) Identification and characterization of the single channel function of human mucolipin-1  
417 implicated in mucopolipidosis type IV, a disorder affecting the lysosomal pathway. *FEBS Lett* 532:  
418 183-187

419 Morales-Perez CL, Noviello CM, Hibbs RE (2016) Manipulation of Subunit Stoichiometry in  
420 Heteromeric Membrane Proteins. *Structure* 24: 797-805  
421 Nagata K, Zheng L, Madathany T, Castiglioni AJ, Bartles JR, García-Añoveros J (2008) The  
422 varitint-waddler (Va) deafness mutation in TRPML3 generates constitutive, inward rectifying  
423 currents and causes cell degeneration. *Proc Natl Acad Sci U S A* 105: 353-358  
424 Nakane T, Kotecha A, Sente A, McMullan G, Masiulis S, Brown P, Grigoras IT, Malinauskaite L,  
425 Malinauskas T, Miehl J *et al* (2020) Single-particle cryo-EM at atomic resolution. *Nature* 587:  
426 152-156  
427 Nilius B, Owsianik G, Voets T, Peters JA (2007) Transient receptor potential cation channels in  
428 disease. *Physiol Rev* 87: 165-217  
429 Pettersen EF, Goddard TD, Huang CC, Couch GS, Greenblatt DM, Meng EC, Ferrin TE (2004)  
430 UCSF Chimera--a visualization system for exploratory research and analysis. *J Comput Chem*  
431 25: 1605-1612  
432 Prat Castro S, Kudrina V, Jašlan D, Böck J, Scotto Rosato A, Grimm C (2022)  
433 Neurodegenerative Lysosomal Storage Disorders: TPC2 Comes to the Rescue! *Cells* 11  
434 Samie M, Wang X, Zhang X, Goschka A, Li X, Cheng X, Gregg E, Azar M, Zhuo Y, Garrity AG  
435 *et al* (2013) A TRP channel in the lysosome regulates large particle phagocytosis via focal  
436 exocytosis. *Dev Cell* 26: 511-524  
437 Scheres SH (2012) RELION: implementation of a Bayesian approach to cryo-EM structure  
438 determination. *J Struct Biol* 180: 519-530  
439 Schmiege P, Fine M, Blobel G, Li X (2017) Human TRPML1 channel structures in open and  
440 closed conformations. *Nature* 550: 366-370  
441 Schmiege P, Fine M, Li X (2021) Atomic insights into ML-SI3 mediated human TRPML1  
442 inhibition. *Structure*  
443 Schuchman EH (2010) Acid sphingomyelinase, cell membranes and human disease: lessons  
444 from Niemann-Pick disease. *FEBS Lett* 584: 1895-1900  
445 Scotto Rosato A, Montefusco S, Soldati C, Di Paola S, Capuozzo A, Monfregola J, Polishchuk E,  
446 Amabile A, Grimm C, Lombardo A *et al* (2019) TRPML1 links lysosomal calcium to  
447 autophagosome biogenesis through the activation of the CaMKK $\beta$ /VPS34 pathway. *Nature*  
448 *Communications* 10: 5630  
449 Shen D, Wang X, Li X, Zhang X, Yao Z, Dibble S, Dong XP, Yu T, Lieberman AP, Showalter HD  
450 *et al* (2012) Lipid storage disorders block lysosomal trafficking by inhibiting a TRP channel and  
451 lysosomal calcium release. *Nat Commun* 3: 731  
452 Slotte JP (2013) Biological functions of sphingomyelins. *Prog Lipid Res* 52: 424-437  
453 Smart OS, Neduveilil JG, Wang X, Wallace BA, Sansom MS (1996) HOLE: a program for the  
454 analysis of the pore dimensions of ion channel structural models. *J Mol Graph* 14: 354-360, 376  
455 Sun M, Goldin E, Stahl S, Falardeau JL, Kennedy JC, Acierno JS, Jr., Bove C, Kaneski CR,  
456 Nagle J, Bromley MC *et al* (2000) Mucopolipidosis type IV is caused by mutations in a gene  
457 encoding a novel transient receptor potential channel. *Hum Mol Genet* 9: 2471-2478  
458 Venkatachalam K, Wong CO, Zhu MX (2015) The role of TRPMLs in endolysosomal trafficking  
459 and function. *Cell Calcium* 58: 48-56  
460 Vergarajauregui S, Puertollano R (2006) Two di-leucine motifs regulate trafficking of mucolipin-1  
461 to lysosomes. *Traffic* 7: 337-353  
462 Xu H, Delling M, Li L, Dong X, Clapham DE (2007) Activating mutation in a mucolipin transient  
463 receptor potential channel leads to melanocyte loss in varitint-waddler mice. *Proc Natl Acad Sci*  
464 *U S A* 104: 18321-18326  
465 Zhang K (2016) Gctf: Real-time CTF determination and correction. *J Struct Biol* 193: 1-12  
466 Zhang X, Chen W, Gao Q, Yang J, Yan X, Zhao H, Su L, Yang M, Gao C, Yao Y *et al* (2019)  
467 Rapamycin directly activates lysosomal mucolipin TRP channels independent of mTOR. *PLoS*  
468 *Biol* 17: e3000252

469 Zhang X, Li X, Xu H (2012) Phosphoinositide isoforms determine compartment-specific ion  
470 channel activity. *Proc Natl Acad Sci U S A* 109: 11384-11389  
471 Zheng SQ, Palovcak E, Armache JP, Verba KA, Cheng Y, Agard DA (2017) MotionCor2:  
472 anisotropic correction of beam-induced motion for improved cryo-electron microscopy. *Nat*  
473 *Methods* 14: 331-332  
474 Zivanov J, Nakane T, Forsberg BO, Kimanius D, Hagen WJ, Lindahl E, Scheres SH (2018) New  
475 tools for automated high-resolution cryo-EM structure determination in RELION-3. *Elife* 7  
476



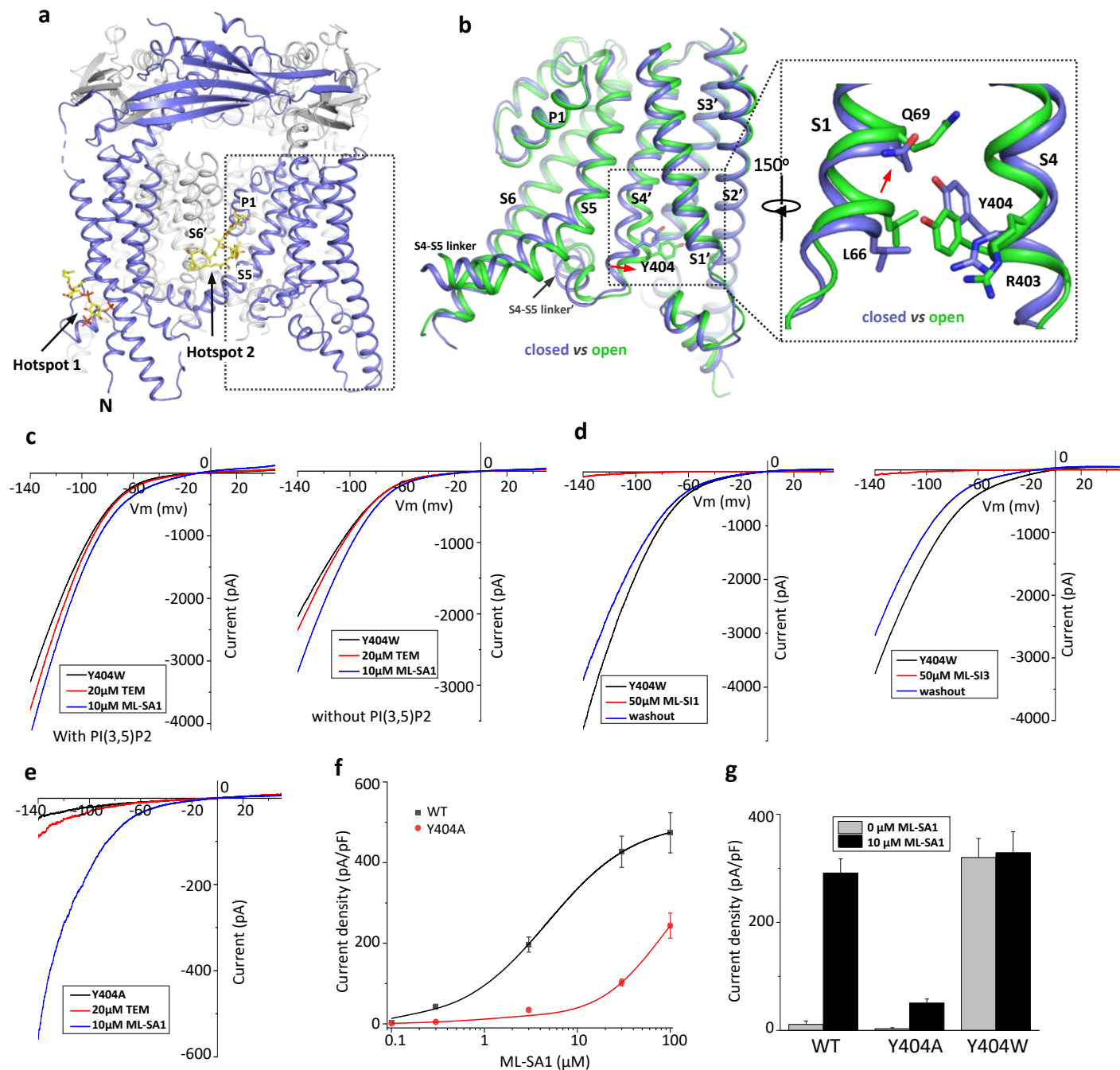


**Figure 1 Design and characterization of allosteric mutations at Tyr404 that recapitulate TRPML1 gating.** (a)

The structure of PI(3,5)P<sub>2</sub>/Temsirrolimus-activated TRPML1 (PDB code:7SQ9) illustrating the two hot spots for ligand binding. Temsirolimus (Tem) is a rapamycin analog. (b) Ligand-induced conformational change and the zoomed-in view of the Y404 movement. Only the boxed region in (a) is shown in the structural comparison between the open (green) and closed (blue) structures. Red arrows mark the bending of S4 and upward movement of S1. (c) Sample traces of Y404W gain-of-function mutant recorded using patch clamp in whole-cell configuration with (left) or without (right) 100 μM PI(3,5)P<sub>2</sub> in the pipette (cytosolic). Tem or agonist ML-SA1 was introduced in the bath solution (extracellular/luminal). (d) Sample traces of Y404W inhibition by antagonists ML-SI1 (left) and ML-SI3 (right) recorded using patch clamp in whole-cell configuration. The antagonists were introduced in the bath solution (extracellular/luminal). (e) Sample traces of Y404A loss-of-function mutant with 100 μM PI(3,5)P<sub>2</sub> in the pipette (cytosolic). Tem or ML-SA1 was introduced in the bath solution (extracellular/luminal). (f) ML-SA1 activation of TRPML1(WT) and Y404A mutant measured at -140 mV. Data for WT is least square fits to the Hill equation with EC<sub>50</sub>=4.8±0.7 μM, n=0.93±0.10. Data points are mean ± SEM (n=5 independent experiments). (g) Current density of wild-type and mutant TRPML1 at -140mV with and without 10μM ML-SA1. Data points are mean ± SEM (n=5 independent experiments)

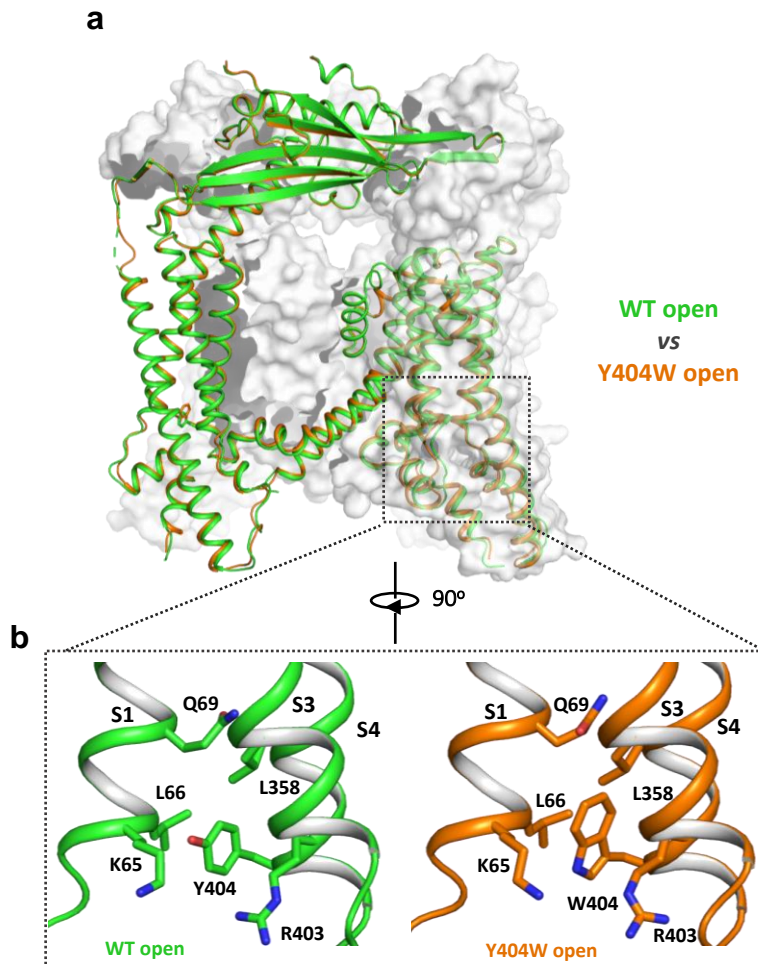


**Figure 2. Y404W mutant adopts an open conformation in the absence of ligands. (a)** Structural comparison between PI(3,5)P<sub>2</sub>/Tem-bound open structure (green) and the Y404W mutant structure (orange). Only the front subunit and the neighboring S1-S4 regions are highlighted in color for clarity. **(b)** Zoomed-in views of the regions surrounding Y404 (WT, green) and W404 (mutant, orange).

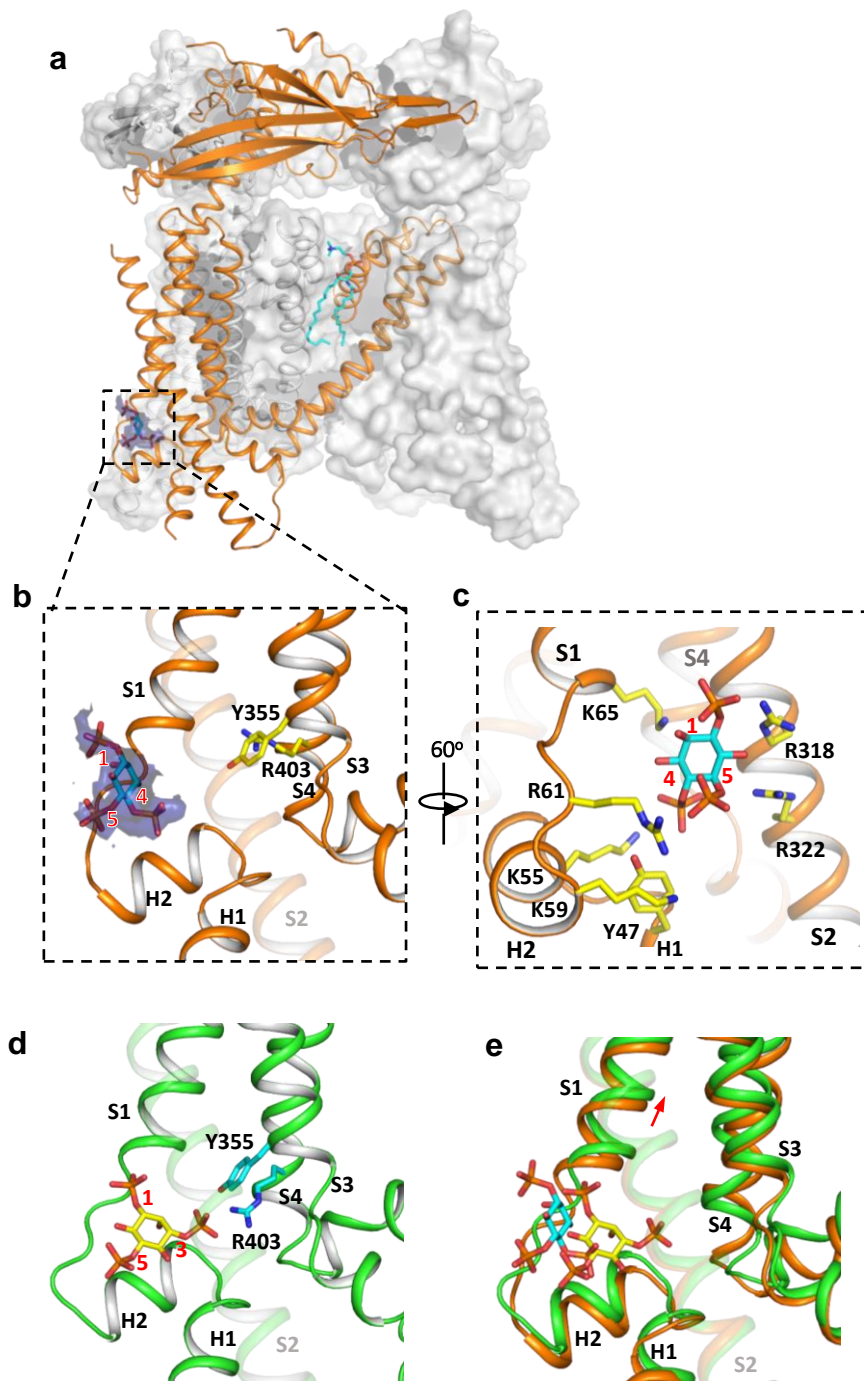


**Figure 3. Structure of TRPML1 in complex with PI(4,5)P<sub>2</sub>.** (a) Overall structure of PI(4,5)P<sub>2</sub>-bound TRPML1 with the front subunit shown in orange cartoon and the rest shown as grey surface representation. Density for PI(4,5)P<sub>2</sub> head group is shown in blue surface. (b) Zoomed-in view of the PI(4,5)P<sub>2</sub>-binding pocket with the density of its IP<sub>3</sub> head group shown in blue surface. (c) Zoomed-in view of the PI(4,5)P<sub>2</sub>-binding pocket with side chains of IP<sub>3</sub>-interacting residues shown as yellow sticks. (d) Zoomed-in view of the IP<sub>3</sub> position in the PI(3,5)P<sub>2</sub>-bound open TRPML1 structure. The C3 phosphate group directly interacts with Y355 and R403. (e) Comparison of the head group positions in PI(3,5)P<sub>2</sub>-bound open (green) and PI(4,5)P<sub>2</sub>-bound closed (orange) structures. The inositol rings PI(3,5)P<sub>2</sub> and PI(4,5)P<sub>2</sub> are colored yellow and cyan, respectively. The red arrow marks the upward movement of S1 from closed to open conformation.

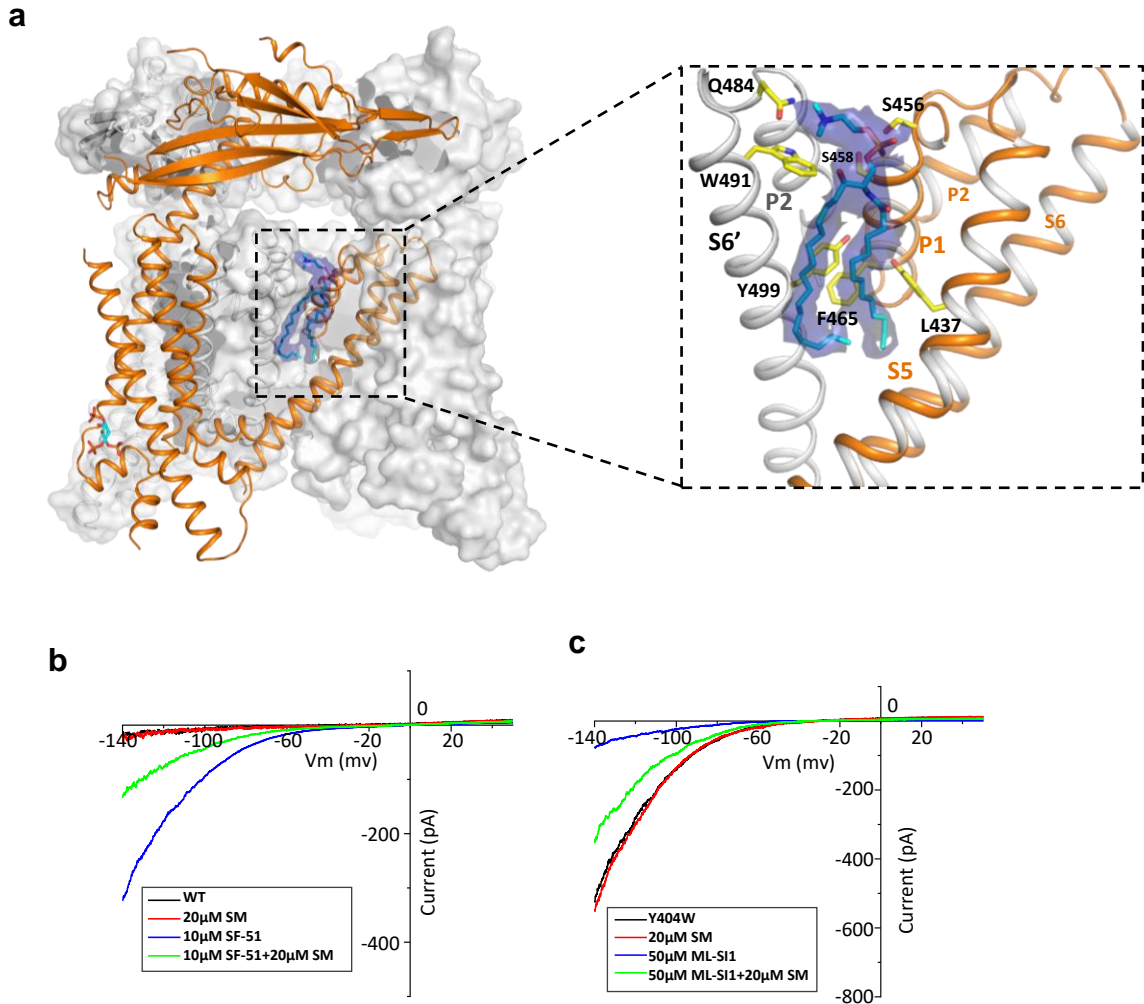


**Figure 4. Sphingomyelin binding in TRPML1.** (a) Overall structure of PI(4,5)P<sub>2</sub>-bound TRPML1 and the zoomed-in view of the lipid-binding site. The lipid density is shown as blue surface and modeled as sphingomyelin (SM). The side chains of lipid-interacting residues are shown as yellow sticks. (b) SM inhibition effect on SF-51-activated wild-type TRPML1. (c) SM activation effect on ML-SI1-inhibited Y404W mutant. Currents shown in (b) and (c) were recorded using patch clamp in whole-cell configuration with pH 4.6 in the bath solution as the adverse effect of SM on agonist or antagonist is subtle and is measurable only at low luminal pH.

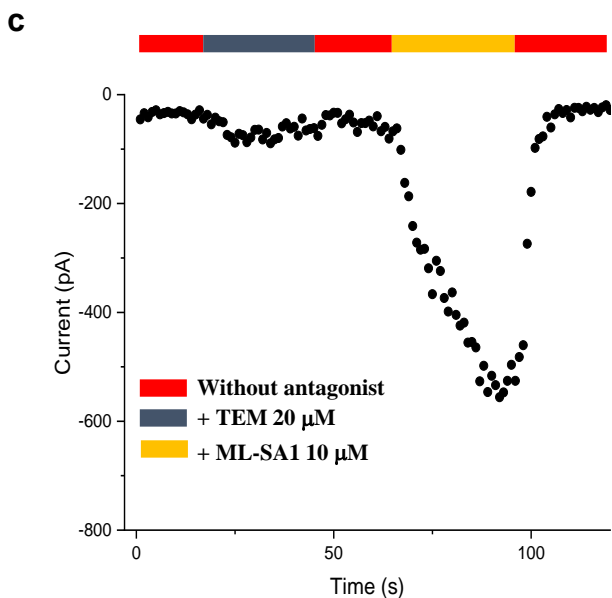
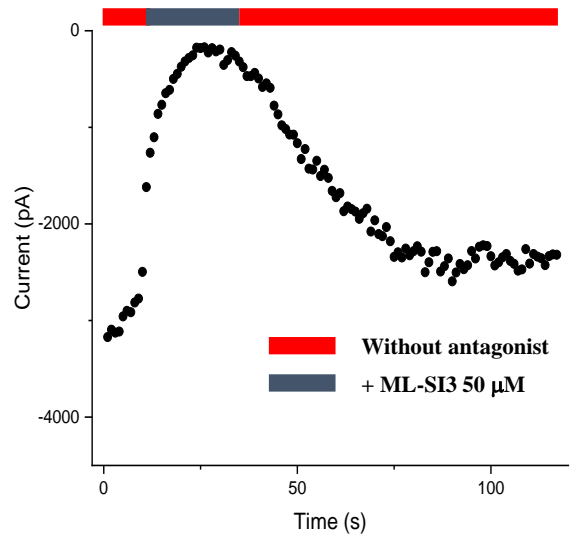
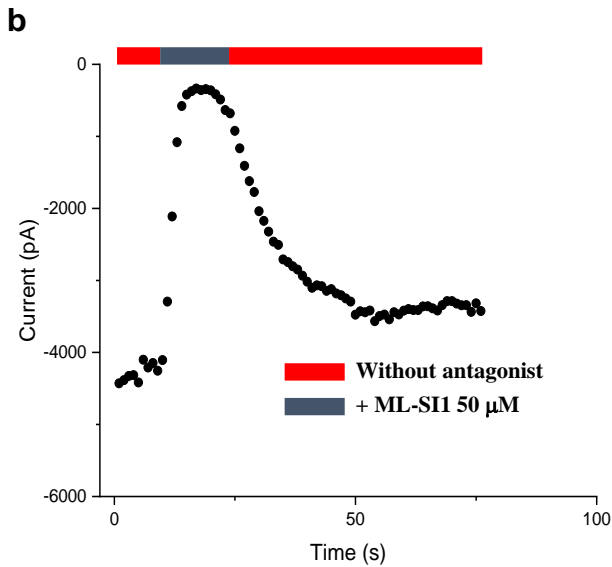
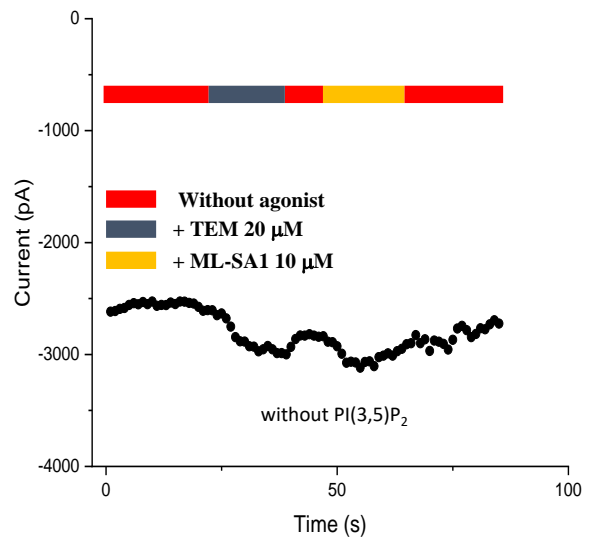
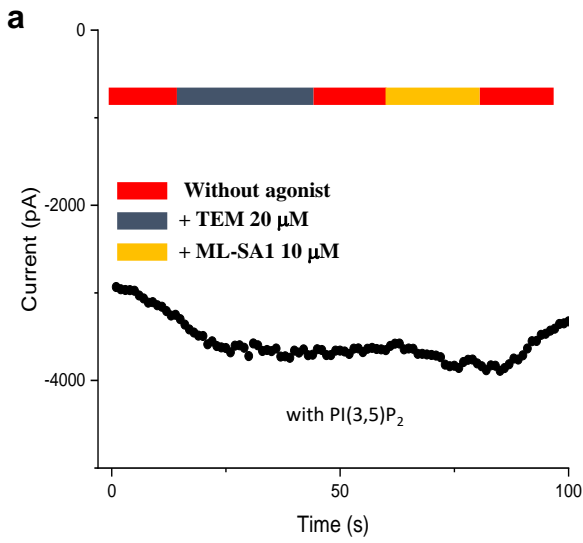


**Figure supplement 1: Time course plots of current amplitudes of Y404 mutations recorded at -140mV with symmetrical pH of 7.4.** (a) Time course plots of Y404W recorded using patch clamp in whole-cell configuration with (left) or without (right) 100 μM PI(3,5)P<sub>2</sub> in the pipette (cytosolic). Tem or agonist ML-SA1 was introduced in the bath solution (extracellular/luminal). (b) Time course plots of Y404W inhibition by antagonists ML-SI1 (left) and ML-SI3 (right) recorded using patch clamp in whole-cell configuration. The antagonists were introduced in the bath solution (extracellular/luminal). (c) Time course plots of Y404A with 100 μM PI(3,5)P<sub>2</sub> in the pipette (cytosolic). Tem or ML-SA1 was introduced in the bath solution (extracellular/luminal).

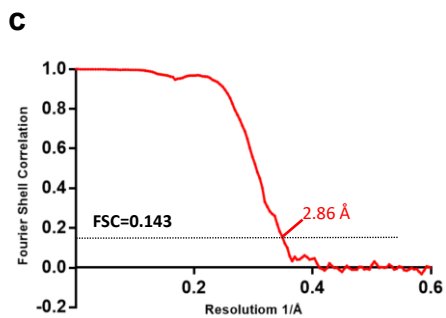
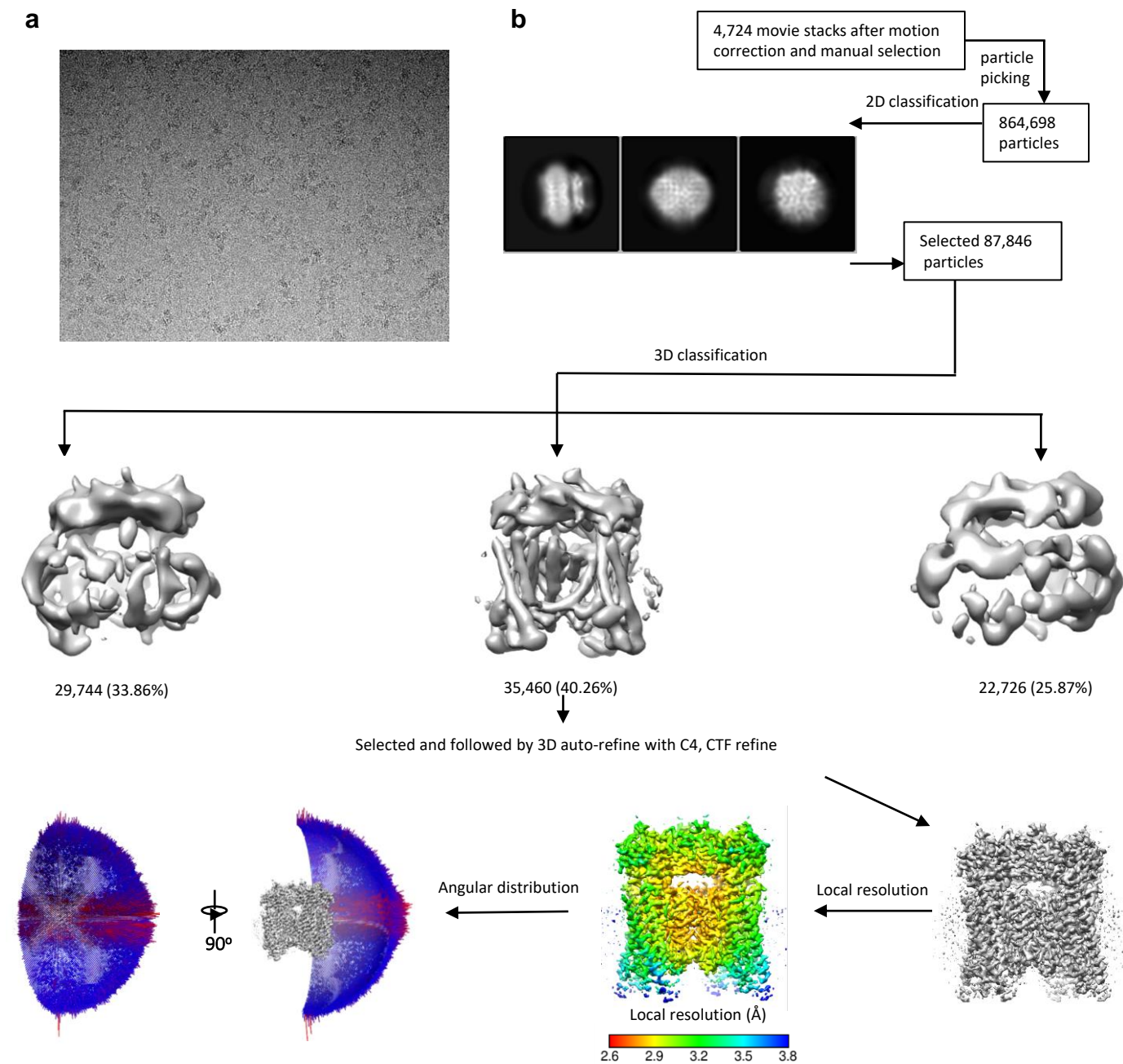


**Figure supplement 2: Cryo-EM data processing scheme of the TRPML1 Y404W.** (a) Representative micrograph. (b) Flow chart of the cryo-EM data processing procedure and the Euler angle distribution of particles used in the final three-dimensional reconstruction. Selected 2D class averages are shown. The final structure represent an open state. (c) Fourier Shell Correlation curves showing the overall resolution at FSC=0.143.

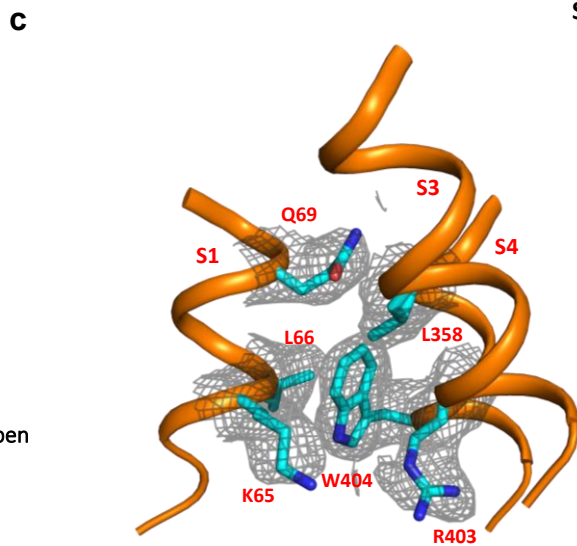
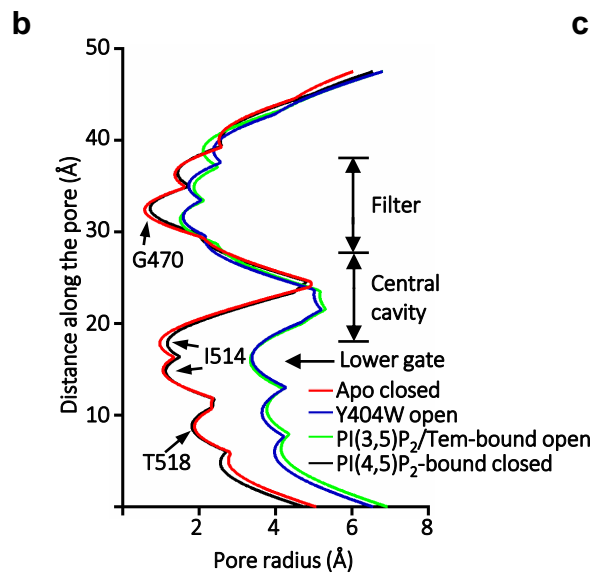
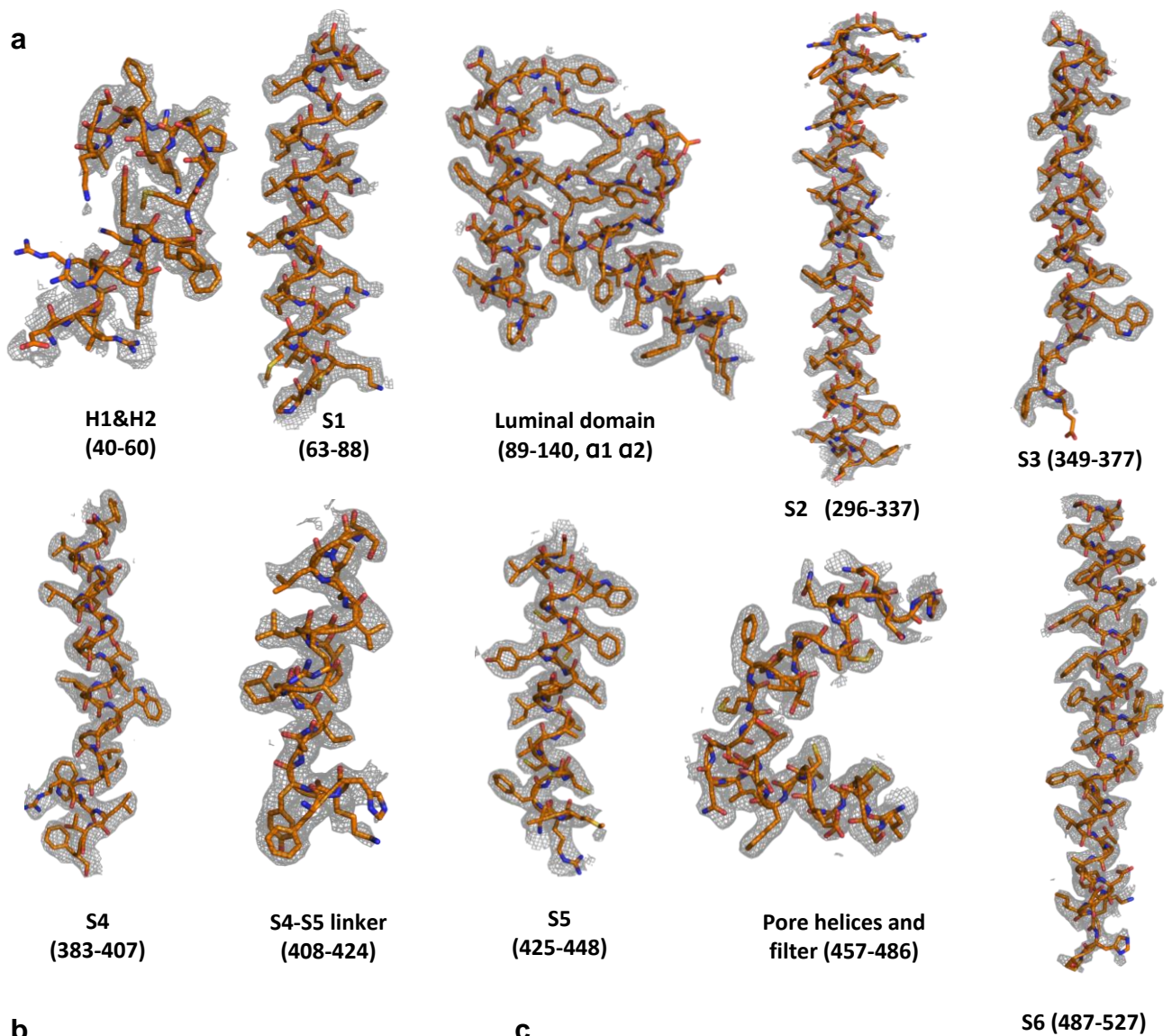


**Figure supplement 3: Sample density maps of Y404W and pore radius:** (a) Sample density maps of the Y404W open TRPML1 structure contoured at  $4\sigma$ . (b) Pore radius along the central axis in the open and closed states. PDB codes for apo closed and PI(3,5)P<sub>2</sub>/Tem-bound open are 7SQ8 and 7SQ9, respectively. (c) EM density map surrounding W404 region shown in grey mesh and contoured at  $4\sigma$ , key W404-interacting residues are shown in cyan. The local resolution of this region is 3.2 Å.

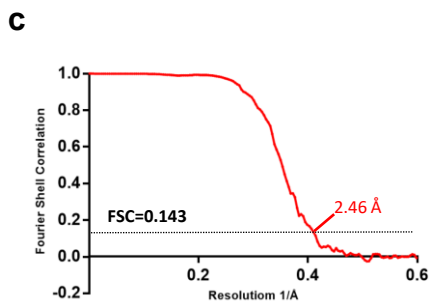
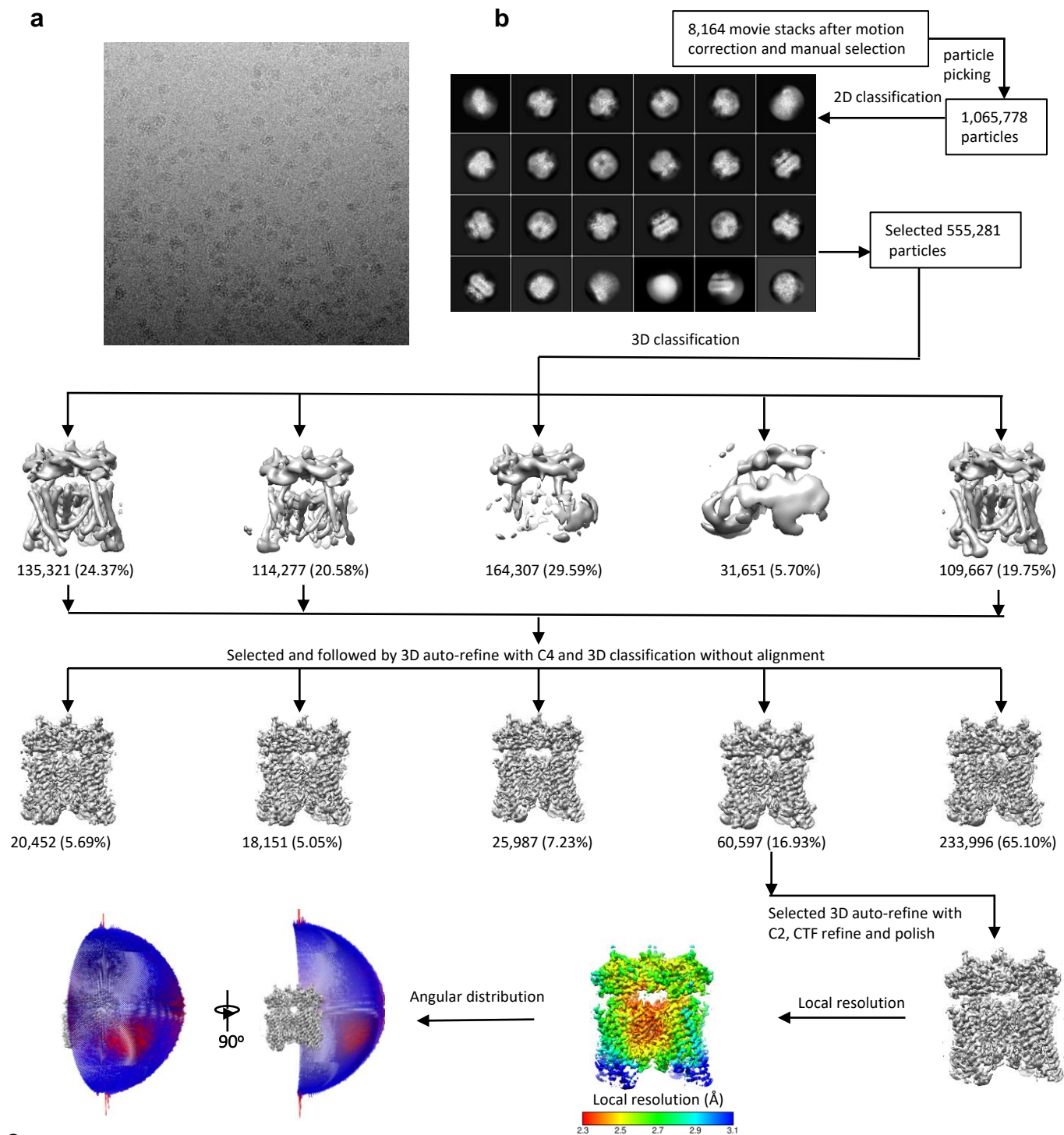


**Figure supplement 4: Cryo-EM data processing scheme of the TRPML1 sample prepared in the presence of PI(4,5)P<sub>2</sub>.** (a) Representative micrograph. (b) Flow chart of the cryo-EM data processing procedure and the Euler angle distribution of particles used in the final three-dimensional reconstruction. Selected 2D class averages are shown. The final structure represent an open state. (c) Fourier Shell Correlation curves showing the overall resolution at FSC=0.143.



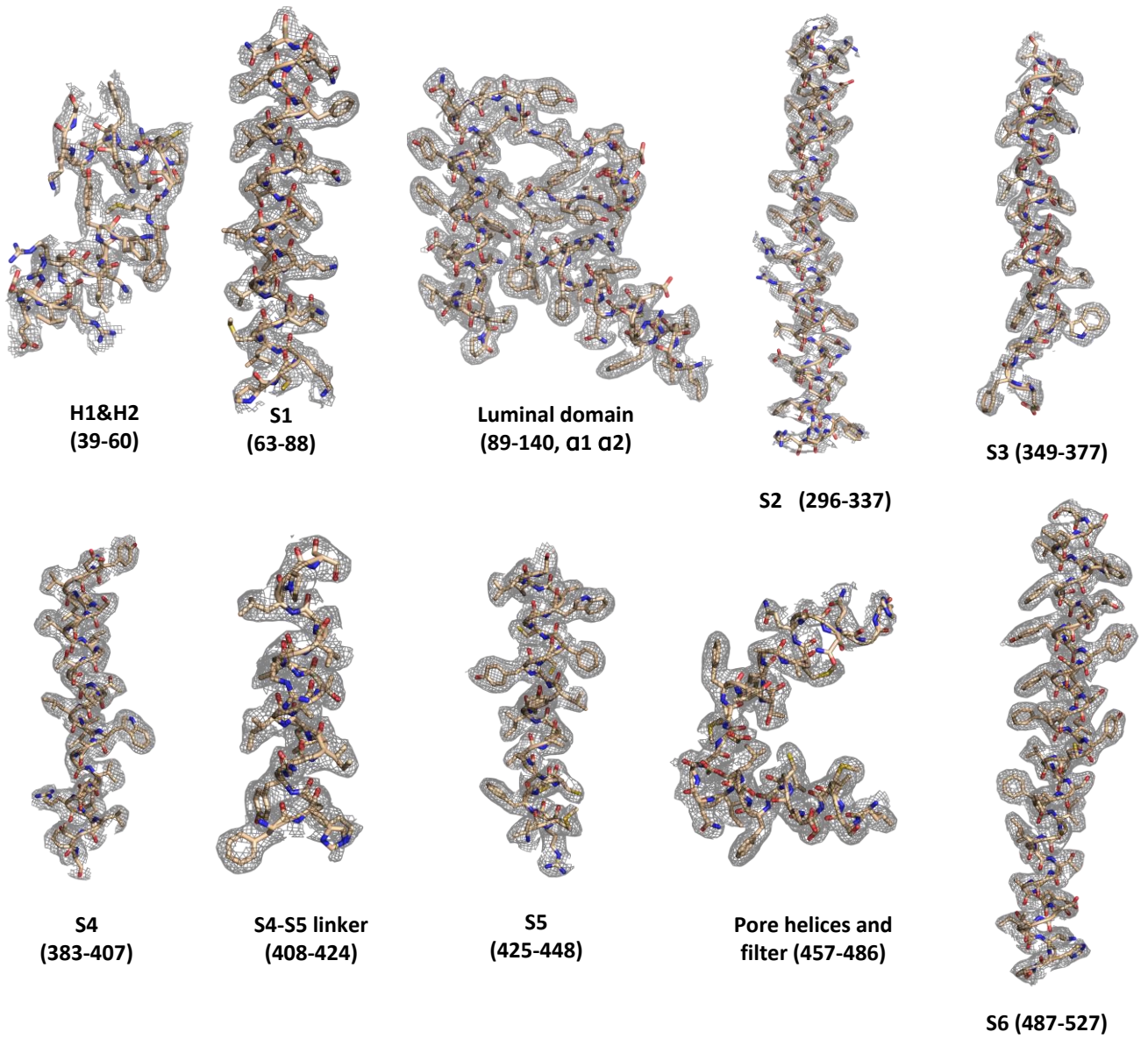


**Figure supplement 5** : Sample density maps of the PI(4,5)P<sub>2</sub>-bound closed TRPML1 structure contoured at 4  $\sigma$ .

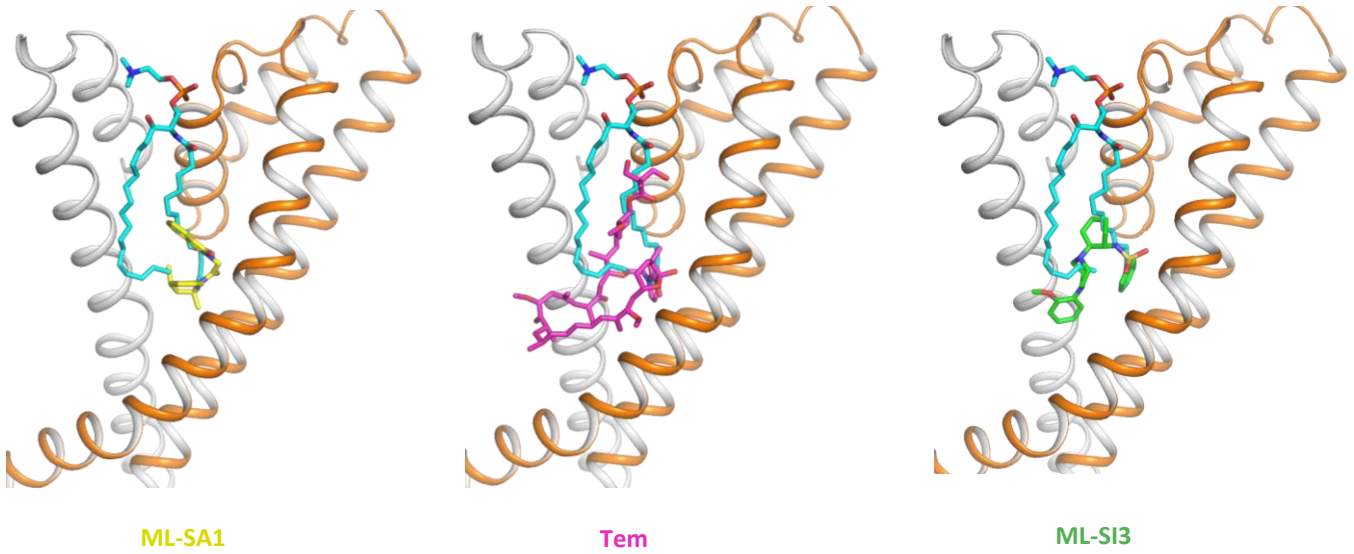


**Figure supplement 6:** Spingomyelin (cyan) binding overlaps with that of agonist ML-SA1 (yellow), rapamycin analog Tem (magenta), or antagonist ML-SI3 (green).

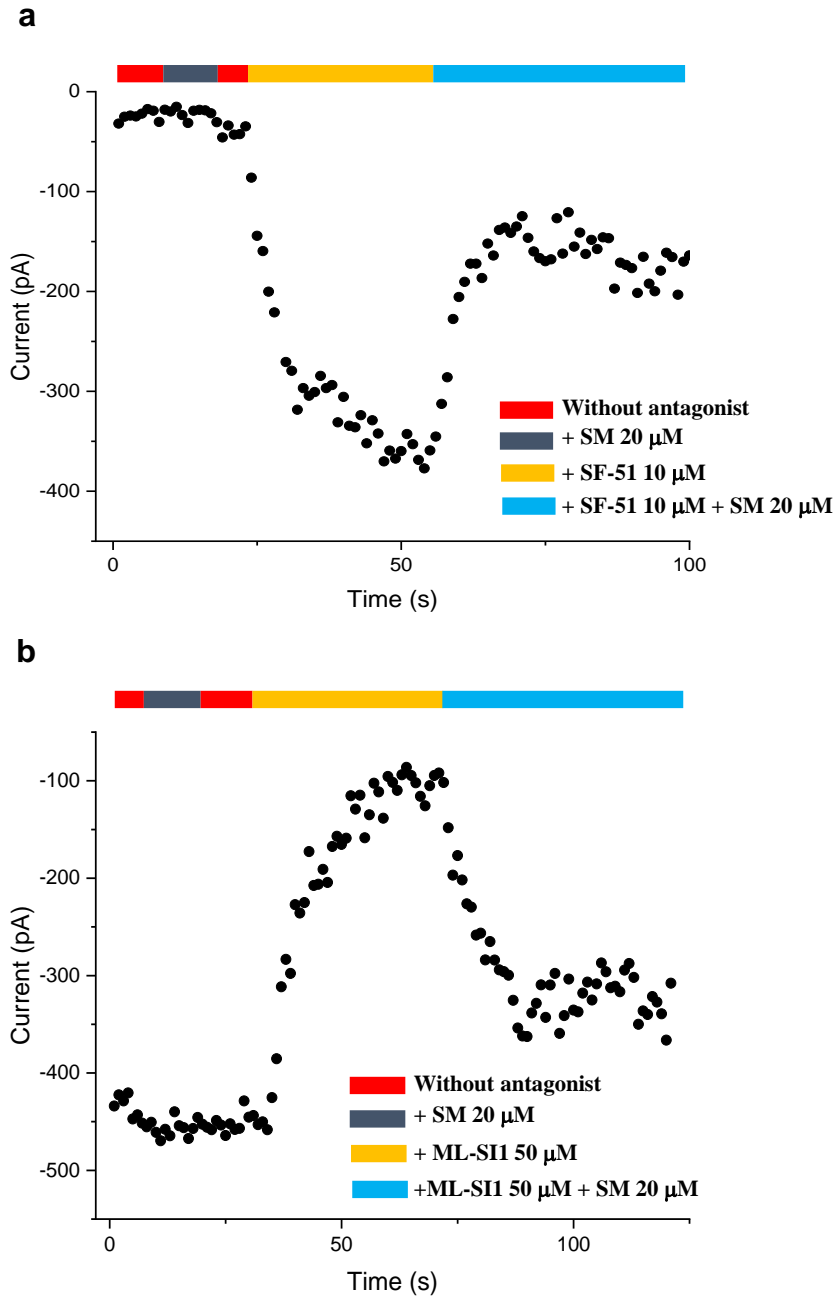


**Figure supplement 7: Time course plots of sphingomyelin affected TRPML1 current amplitudes.** (a) Sphingomyelin inhibition effect on SF-51-activated wild-type TRPML1. (b) SM activation effect on ML-SI1-inhibited Y404W mutant. Currents shown in (a) and (b) were recorded at -140mV using patch clamp in whole-cell configuration with pH 4.6 in the bath solution as the adverse effect of SM on agonist or antagonist is subtle and is measurable only at low luminal pH.

**Top View**



**Movie supplement 1. Conformational changes between open and closed TRPML1**